Letter Vol. 46, No. 5 / 1 March 2021 / Optics Letters 1013

Optics Letters

Transient-grating single-shot supercontinuum spectral interferometry (TG-SSSI)

S. W. Hancock, S. Zahedpour, and H. M. Milchberg*

Institute for Research in Electronics and Applied Physics, University of Maryland, College Park, Maryland 20742, USA
**Corresponding author: milch@umd.edu*

Received 16 December 2020; revised 24 January 2021; accepted 26 January 2021; posted 27 January 2021 (Doc. ID 417803); published 18 February 2021

We present a technique for the single-shot measurement of the spatiotemporal (1D space + time) amplitude and phase of an ultrashort laser pulse. The method, transient grating single-shot supercontinuum spectral interferometry (TG-SSSI), is demonstrated by the space–time imaging of short pulses carrying spatiotemporal optical vortices. TG-SSSI is well suited for characterizing ultrashort laser pulses that contain singularities associated with spin/orbital angular momentum or polarization.

https://doi.org/10.1364/OL.417803

The need to characterize ultrashort laser pulses has spawned a large and increasing number of single-shot techniques, including autocorrelation [1], multiple versions of frequency resolved optical gating (FROG) [2–6], spectral phase interferometry for direct electric field reconstruction (SPIDER) and related methods [7–12], STRIPED FISH [13], d-scan [14], plus single-shot supercontinuum spectral interferometry (SSSI) [15–17], and other spectral interferometry methods [18,19]. While the basic FROG and SPIDER techniques extract only the space-independent temporal amplitude and phase, more complicated techniques [12–14] have recovered the *spatiotemporal* phase and amplitude of a laser pulse in a single-shot, albeit only with simple features such as pulse front tilt. STRIPED-FISH [13] and d-scan [14] methods use iterative algorithms which, to the best of our knowledge, have not been shown to converge for complicated structured light containing singularities, and SEA-SPIDER requires ancillary assumptions in determining the timing of spatial slices [12]. While SSSI does not recover the spatiotemporal phase of a pulse, it does recover the spatiotemporal pulse envelope, which has enabled measurement of ionization rates and ultrafast plasma evolution [20], electronic, vibrational and rotational nonlinearities [21,22], as well as nonlinear refractive indices and pulse front tilt [23].

In this Letter, we present a new method that can measure, in a single-shot, the spatiotemporal phase and amplitude of an ultrafast laser pulse. It was developed for recent measurements [24] of pulses embedded with spatiotemporal optical vortices (STOVs) [25] and is well suited for characterizing ultrashort laser pulses that contain singularities associated with spin/orbital angular momentum [26–28] or polarization [29].

We first briefly review SSSI by examining three of the beams in Fig. 1(a): the "structured pulse" E_S which we want to measure, the reference pulse $E_{\rm ref}$, and the probe pulse $E_{\rm pr}$. Here the structured pulse has spatiotemporal phase and amplitude imposed by the zero dispersion $4f$ pulse shaper [30–32] in Fig. 1(b). The reference and probe supercontinuum (SC) pulses are generated upstream of Fig. 1(a) by filamentation in a 2 atm SF_6 cell followed by a Michelson interferometer (not shown), with $E_{\rm ref}$ leading $E_{\rm pr}$ by ~ 2 ps. The transient amplitude of E_S is measured via the phase modulation it induces in a spatially and temporally overlapped SC probe pulse $E_{\rm pr}$ in an instantaneous Kerr "witness plate," here a thin (100–500 μm) fused silica window. E_S is sufficiently weak and/or the witness plate is sufficiently thin that E_S does not propagate nonlinearly. (Its own phase fronts are negligibly perturbed.) The resulting spatio-spectral phase shift $\Delta\varphi(x,\omega)$ imposed on the probe is extracted from interfering $E_{\rm pr}^{\rm out} \sim \chi^{(3)} E_S E_S^* E_{\rm pr}^{\rm in}$ with $E_{\rm ref}$ in an imaging spectrometer. Here $E_{\rm pr}^{\rm in}$ and $E_{\rm pr}^{\rm out}$ are the probe fields entering and exiting the witness plate, $\chi^{(3)}$ is the fused silica nonlinear susceptibility, and x is the position within a 1D transverse spatial slice through the pump pulse at the witness plate (axes shown in Fig. 1). Fourier analysis of the extracted $\Delta\varphi(x,\omega)$ [20] then determines the spatiotemporal phase shift $\Delta\phi(x,\tau) \propto |E_S(x,\tau)|^2 \propto I_S(x,\tau)$, yielding the 1D space + time spatiotemporal intensity envelope I_S.

Measurement of the spatiotemporal phase of E_S is enabled by the addition of an interferometric reference pulse $\mathcal{E}_i$, which is crossed with E_S at a small angle θ_i. ($\theta_w = 3.15°$ in the witness plate.) This forms a nonlinear transient refractive index grating, where $\mathcal{E}_i$ has the same center wavelength as E_S, but is bandpassed to be temporally longer. The transient grating (TG) is now the signal probed by SSSI (yielding the new method we call transient grating single-shot supercontinuum spectral interferometry [TG-SSSI]), where the output probe pulse from the witness plate becomes $E_{\rm pr}^{\rm out} \propto \chi^{(3)}(|E_s|^2 + |\mathcal{E}_i|^2 + E_s^*\mathcal{E}_i + E_S\mathcal{E}_i^*)E_{\rm pr}^{\rm in}$. A chopper on the E_S beam path (but not on the $\mathcal{E}_i$ beam path) enables the $\chi^{(3)}|\mathcal{E}_i|^2$ signal contribution to be subtracted out as background on every other shot. The interference of $E_{\rm pr}^{\rm out}$ and $E_{\rm ref}$ in the imaging spectrometer then enables extraction of $\Delta\varphi(x,\omega)$, yielding $\Delta\phi(x,\tau)$ as before. We note that $\Delta\phi(x,\tau) \propto |E_S(x,\tau)|^2 + 2|E_S||\mathcal{E}_i| f(x,\tau)$, where the TG

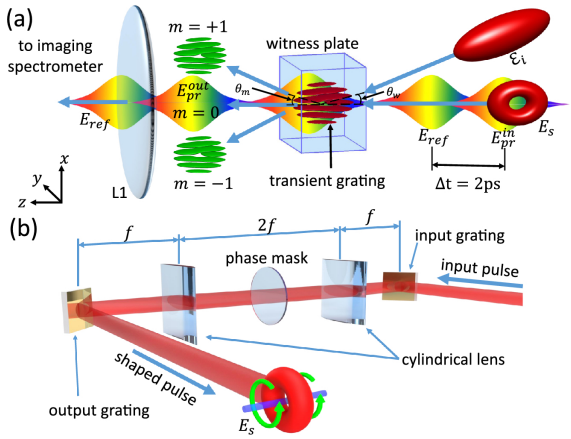

Fig. 1. (a) Setup for TG-SSSI. The structured pulse E_S and the interferometric reference pulse $\mathcal{E}_i$ cross at angle θ_w in a fused silica witness plate, forming a transient grating. The grating is probed by a SC probe $E_{\text{pr}}^{\text{in}}$, preceded ~ 2 ps earlier by a reference SC pulse E_{ref}. Imaged by L1, E_{ref} and $E_{\text{pr}}^{\text{out}}$ interfere at an imaging spectrometer, and the interferogram is analyzed in the Fourier domain, yielding a single-shot time and space resolved image of amplitude and phase of E_S. (b) $4f$ pulse shaper [30–32] for generating spatiotemporally structured pulses E_S, here STOVs [24,33,34], imposed on a 50 fs, $\lambda = 800$ nm input pulse. The STOV phase windings are imposed by $l = \pm 1$ and $l = -2$ spiral phase plates in the Fourier plane of the pulse shaper. The phase plates are etched on fused silica and have 16 levels (steps) every 2π.

is $f(x, \tau) = \cos(2k_w x \sin(\theta_w/2) + \Delta\Phi(x, \tau))$, $k_w = n_0 k$ is the pump central wavenumber in the witness plate, $n_0 = 1.45$, and $\Delta\Phi(x, \tau)$ is the spatiotemporal phase of E_S with respect to $\mathcal{E}_i$ (reference phase is flat in our case). In the analysis of the 2D $\Delta\phi(x, \tau)$ images, $\Delta\Phi(x, \tau)$ is extracted using standard interferogram analysis techniques [13,14], and $I_S(x, \tau)$ is extracted using a low-pass image filter (suppressing the sidebands imposed by the TG). Due to group velocity mismatch (GVM) in the witness plate between E_S (centre wavelength $\lambda_0 = 800$ nm) and the SC probe ($\lambda_{\text{pr}} = 600$ nm), the extracted phase shift is smeared slightly in time by ~ 4 fs per 100 μm of fused silica. The temporal resolution (here ~ 7 fs) determines the shortest measurable pulse and depends on this GVM and on the sampled bandwidth of E_{pr}. The longest measurable pulse is determined by the duration of the chirped E_{pr}, here ~ 1 ps. For weak E_S pulses, the focusing can be adjusted and/or the thickness of the witness plate can be increased. Here the minimum E_S pulse energy was 3μJ (~150 GW/cm^2).

The laser used in the experiments is a 4 mJ/pulse, 50 fs FWHM, $\lambda_0 = 800$ nm, 1 kHz Ti:sapphire system. The beam is split three ways, with ~ 100 μJ directed to SC generation (400–700 nm) for E_{pr} and E_{ref}, and a portion of the rest for E_S and $\mathcal{E}_i$, whose energies were controlled using $\lambda/2$ plates and thin-film polarizers. The structured pulse E_S was embedded with spatiotemporal phase windings by placing $l = \pm 1$ or $l = -2$ spiral phase plates at the Fourier plane of the $4f$ pulse shaper [24].

As depicted in Fig. 1, the SC reference and probe pulses, E_{ref} and $E_{\text{pr}}^{\text{in}}$, are combined collinearly with the pulse E_S using a dichroic mirror, with E_S, $\mathcal{E}_i$, and $E_{\text{pr}}^{\text{in}}$ overlapping temporally in the witness plate, while E_{ref} precedes them (by 2 ps). From the output face of the witness plate, E_{ref} and $E_{\text{pr}}^{\text{out}}$ were magnified and relay imaged onto the spectrometer slit using a high numerical aperture (NA) telescope with achromatic lenses. A high NA is necessary to collect the first-order diffraction ($m = \pm 1$) of $E_{\text{pr}}^{\text{out}}$ from the TG. Achromatic imaging is essential for all SC wavelengths to be in focus at the spectrometer slit and to minimize spherical aberration, which could spatially offset the diffracted orders of $E_{\text{pr}}^{\text{out}}$ from the zero order. Background and signal data were collected at 40 Hz by placing a chopper in the path of E_S, which enabled the subtraction of the phase shift induced by $|\mathcal{E}_i|^2$ in the witness plate.

In principle, achromatic imaging of all diffracted orders precludes the need for detailed analysis of the diffraction. However, it is interesting to note that in our experiment, we observe only the zero order ($m = 0$) and the $m = -1$ order diffraction of the probe. To understand this, we assess whether probe diffraction is in the Bragg regime (one dominant diffraction peak) or in the Raman–Nath regime (multiple positive and negative diffraction orders) [35] by considering the dimensionless parameter $Q = 2\pi\lambda_i L/\Lambda^2\bar{n}$, where λ_i is the vacuum wavelength of incident light, Λ is the interference grating period, $\bar{n}$ is the mean refractive index, and L is the grating thickness. From ref. [35], diffraction is in the Raman–Nath regime for $Q \leq 1$ and in the Bragg regime for $Q \gg 1$. Our TG-SSSI configuration (with a $l = 500$ μm fused silica witness plate, $\Lambda(\theta_w = 3.15°) = 10$ μm, $n_2 = 2.5 \times 10^{-16}$ cm^2/W, and $\bar{n} = n_0 + n_0 n_2 I = n_0 + \Delta\phi_{\text{TG}}/kL$, where $\Delta\phi_{\text{TG}}$ is the modulated phase shift amplitude of the TG) gives $Q \cong 13.0$, which is in the Bragg regime. (Both $\Delta\phi_{\text{TG}}$ and Λ are from our measurements.) This explains the observation of only one diffracted order.

This result is confirmed by simulations of scattering of E_{pr} from the nonlinear grating formed by the interference of E_S and $\mathcal{E}_i$. The simulation uses our implementation of the unidirectional pulse propagation equation method [36,37], where all three beams intersect in the 500 μm thick fused silica plate (with E_S and $\mathcal{E}_i$ crossing at angle θ_w and $E_{\text{pr}}^{\text{in}}$ normal to the surface). The beam parameters are E_S ($\lambda = 800$ nm, 50 fs FWHM, $w_0 = 100$ μm, $I_{S,\text{peak}} = 28$ GW/cm^2, $l = +1$ STOV), $\mathcal{E}_i$ ($\lambda = 800$ nm, 300 fs FWHM, $w_0 = 300$ μm, $I_{i,\text{peak}} = 28$ GW/cm^2, GDD = 0 fs^2), and $E_{\text{pr}}^{\text{in}}$ ($\lambda = 600$ nm, $\Delta\lambda = 350$ nm, 2.4 ps FWHM, $w_0 = 500$ μm, GDD = 1200 fs^2, TOD = 200 fs^3). The output electric field is numerically propagated 4 cm beyond the witness plate in air and then E_S and $\mathcal{E}_i$ are spectrally filtered out, leaving the field $E_{\text{pr}}^{\text{out}}$. Figure 2(a) shows simulation results of probe diffraction for conditions similar to our experimental parameters ($\theta_w = 3.15°$ and $Q = 13.0$), where only the $m = -1$ diffraction order is present (Bragg regime), agreeing with our experiments. As a comparison, the crossing angle for Fig. 2(b) was chosen to be $\theta_w = 0.31°$, giving $Q = 0.13$, in the Raman–Nath regime, and the $m = \pm 1$ orders are present. We note that our current TG-SSSI setup could be adjusted to operate in the Raman–Nath regime by increasing the grating period Λ (to $\Lambda \geq \sqrt{(2\pi\lambda_i L/\bar{n})}$), but increasing the intensity of E_S or $\mathcal{E}_i$ to increase n_1 could result in non-negligible plasma formation in the witness plate and refractive distortion of E_{pr}.

Figure 3(a) shows an example of a raw TG-SSSI interferogram frame recorded on the imaging spectrometer camera. Here the pulse shaper generates E_S as a $l = -2$ spatiotemporal optical vortex (STOV) pulse [24,25]. The vertical spectral fringe spacing is set by the Michelson-imposed time delay between the E_{ref} and $E_{\text{pr}}^{\text{out}}$ pulses. As discussed earlier, the 2D phase

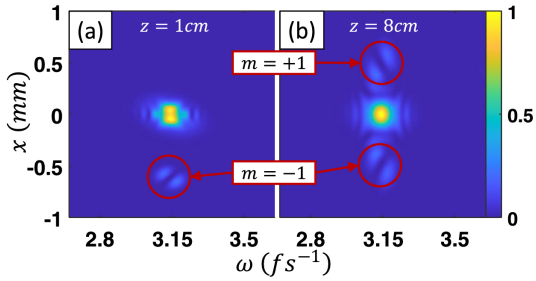

Fig. 2. Simulated spectrally resolved scattering of SC probe pulse E_{pr} from a transient nonlinear grating in a 500 μm thick fused silica plate, generated by the interference of pulses E_S and $\mathcal{E}_i$, where z is distance from the output face of the plate. Plotted as $|\Delta E_{\mathrm{pr}}|^2 = |E_{\mathrm{pr}}^{\mathrm{out}} - E_{\mathrm{pr}}^{\mathrm{in}}|^2$. (a) Bragg regime transient grating: $\theta_w = 3.15°$, grating period $\Lambda = 10$ μm, and $Q = 13.0$. Here the scattering is captured at $z = 1$ cm owing to the rapid escape of the single diffracted order ($m = -1$) from the simulation window. (b) Raman–Nath regime: $\theta_w = 0.31°$, $\Lambda = 100$ μm, and $Q = 0.13$, showing $m = \pm 1$ diffraction orders.

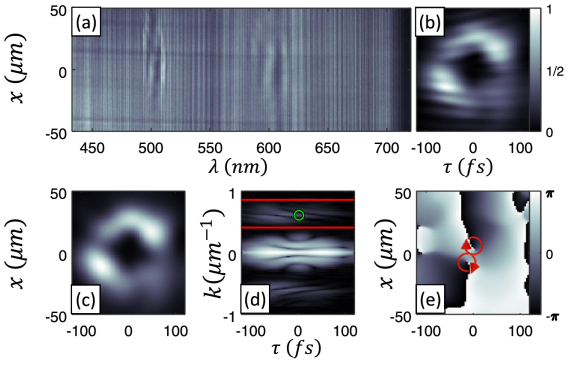

Fig. 3. Measurement of a $l = -2$ STOV-carrying pulse (interferometric reference $\mathcal{E}_i$ at 800 and 10 nm FWHM bandwidth). (a) Raw 1D space resolved spectral interferogram; (b) extracted $\Delta\phi(x, \tau)$; (c) pulse envelope $I_S(x, \tau)$ from low-pass filtering of $\Delta\phi(x, \tau)$; (d) $\log(|\mathcal{F}_x\{\Delta\phi(x, \tau)\}| + 1)$. The red lines show the region to be spectrally windowed, and the green circle identifies (k_c, τ_c) for frame averaging; (e) extracted spatiotemporal phase of the pulse, $\Delta\Phi(x, \tau)$.

shift $\Delta\varphi(x, \omega)$ is extracted in the same way as that of all other SSSI interferograms [14,15], yielding $\Delta\phi(x, \tau)$, as plotted in Fig. 3(b). Here the horizontal fringes imposed by $f(x, \tau)$ show the time-dependent interference between E_S and $\mathcal{E}_i$. The spatiotemporal pulse envelope is recovered by low-pass image filtering of $\Delta\phi(x, \tau)$ to remove $f(x, \tau)$, yielding $I_s(x, \tau)$ in Fig. 3(c).

Extraction of the spatiotemporal phase $\Delta\Phi(x, \tau)$ is performed by Fourier analysis along x [38]:

$$\Delta\Phi(x, \tau) = \arg\left(\mathcal{F}_k^{-1}\{\mathcal{F}_x\{\Delta\phi(x, \tau)\}\Theta(k)\}\right), \quad (1)$$

where $\mathcal{F}_x\{\Delta\phi(x, \tau)\} = \Delta\tilde{\phi}(k, \tau)$ is the Fourier transform along x, $\mathcal{F}_k^{-1}\{\cdot\}$ is the inverse Fourier transform along k, $\Theta(k)$ is a sideband windowing and shifting ($k \to k - 2\pi/\Lambda$) function, and k is the x-component of the spatial frequency. This is shown in Figs. 3(d) and 3(e). If the sideband is too close to the k-spectrum of the pulse envelope (which is centered at $k = 0$), $\Theta(k)$ cannot separate the TG from the pulse envelope. This necessitates a larger spatial sample and/or finer grating period, considerations that have informed our pump–probe beam geometry.

While the single-shot signal-to-noise ratio is ∼4:1, we perform 500 frame averages to enhance it to ∼80:1. Before averaging, however, the shot-to-shot shifting of the spatial interference fringes (from mechanical vibrations in the optical setup) must be compensated. The fringes are effectively forced into common alignment by adding a constant phase $\Delta\tilde{\phi}_n(k_c, \tau_c)$ to each frame, giving

$$\Delta\Phi(x, \tau) = \arg\left(\frac{1}{N}\sum_{n=1}^{N}\mathcal{F}_k^{-1}\left\{\left[\Delta\tilde{\phi}_n(k, \tau) \times \exp(i\arg(\Delta\tilde{\phi}_n(k_c, \tau_c)))\right]\Theta(k)\right\}\right), \quad (2)$$

where $\Delta\tilde{\phi}_n(k, \tau) = \mathcal{F}_x\{\Delta\phi_n(x, \tau)\}$, $\Delta\tilde{\phi}_n(k_c, \tau_c)$ is the constant phase added to frame n to align the fringes, (k_c, τ_c) is a common point across all N frames, and $\Delta\phi(x, \tau)$ is the mean spatiotemporal phase. The point (k_c, τ_c) is chosen at a location in the sideband where the signal is sufficiently larger than the phase noise; otherwise, each frame would be offset by a random phase factor.

To demonstrate TG-SSSI, we used the $4f$ pulse shaper to generate (a) a Gaussian pulse ($l = 0$, no phase plate) and STOV-carrying pulses with topological charge (b) $l = +1$, (c) $l = -1$, and (d) $l = -2$, using corresponding spiral phase plates in the Fourier plane of the shaper. The columns of Fig. 4 show $\Delta\phi(x, \tau)$, $I_s(x, \tau)$, $f(x, \tau)$, and $\Delta\Phi(x, \tau)$ for pulses carrying $l = 0, \pm 1$, and -2. For $l = 0$ (row (a)), we see a slight fringe curvature in the TG $f(x, \tau)$, indicating a dispersion mismatch between E_S and $\mathcal{E}_i$. For the $l = \pm 1$ STOVs in rows (b) and (c), $f(x, \tau)$ clearly shows the transient fringe fusing or splitting, identifying the opposite phase windings shown in the $\Delta\Phi(x, \tau)$ column. For $l = -2$ (row (d)), one fringe in $f(x, \tau)$ splits

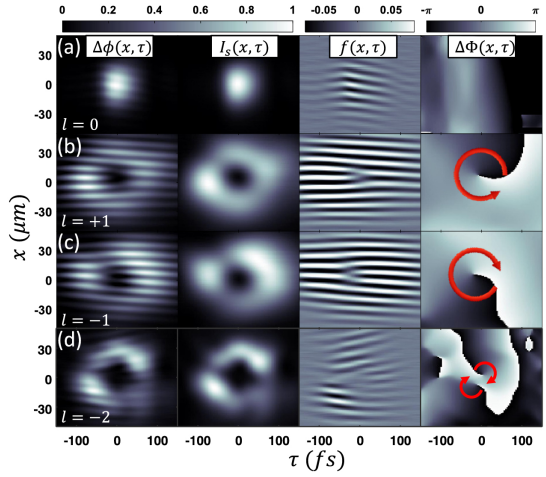

Fig. 4. Experimental results from TG-SSSI after fringe alignment. The columns show the extracted full TG-SSSI signal $\Delta\phi(x, \tau)$, which is low-pass filtered to yield the pulse intensity envelope $I_s(x, \tau)$, or high-pass filtered to give the transient grating $f(x, \tau)$, from which the spatiotemporal phase $\Delta\Phi(x, \tau)$ is extracted. The rows show the results for (a) a Gaussian pulse ($l = 0$), (b) a $l = +1$ STOV, (c) a $l = -1$ STOV, and (d) results from an $l = -2$ phase plate. The red arrows denote the direction of the increasing spatiotemporal phase.

into three at the center of the pulse. Upon phase extraction, $\Delta\Phi(x, \tau)$ has two nearby $l = -1$ phase windings rather than a single $l = -2$ winding. We attribute this to a mismatch between the transverse beam dimensions at the Fourier plane of the pulse shaper and the radially independent phase winding of the $l = -2$ phase plate. Since the profile of the beam in the Fourier plane of the shaper (itself dictated by the grating periodicity and cylindrical lens focal length) is slightly elliptical, one of the axes of the phase plate should ideally be scaled to match the ellipticity of the beam. Utilizing a programmable spatial light modulator rather than a fixed phase plate in the pulse shaper would enable scaling of the phase plate to match the beam profile, making possible the generation of $l = \pm 2$ and even higher-order STOVs. Finally, we note that, for experiments where the structured pulse E_S is highly repetitive and reproducible, TG-SSSI could be extended to two spatial dimensions (x and y) by transversely scanning $E_{\mathrm{pr}}^{\mathrm{out}}$ across the spectrometer entrance slit in the y direction, as is done in 2D + 1 SSSI [20], to obtain $I_S(x, y, \tau)$ and $\Delta\Phi(x, y, \tau)$.

In summary, we have presented a new single-shot diagnostic of ultrashort spatiotemporally structured laser pulses, TG-SSSI and have used it to measure simple Gaussian and STOV-carrying pulses generated by a $4f$ pulse shaper. Among multiple possible applications, TG-SSSI should prove useful in the study of nonlinear propagation, collapse, and collapse arrest of intense laser pulses in transparent media, where spatiotemporal optical pulse structures naturally emerge [25]. Recently, we have used TG-SSSI to measure, for the first time, angular momentum conservation in second harmonic generation of STOVs [39, 40].

Funding. National Science Foundation (PHY2010511); Office of Naval Research (N00014-17-1-2705, N00014-20-1-2233); Air Force Office of Scientific Research (FA9550-16-1-0121, FA9550-16-1-0284).

Acknowledgment. The authors thank I. Larkin for discussions and technical assistance.

Disclosures. The authors declare no conflicts of interest.

REFERENCES

1. F. Salin, P. Georges, G. Roger, and A. Brun, Appl. Opt. **26**, 4528 (1987).
2. R. Trebino and D. J. Kane, J. Opt. Soc. Am. A. **10**, 1101 (1993).
3. D. J. Kane and R. Trebino, Opt. Lett. **18**, 823 (1993).
4. J. N. Sweetser, D. N. Fittinghoff, and R. Trebino, Opt. Lett. **22**, 519 (1997).
5. K. W. Delong, R. Trebino, J. Hunter, and W. E. White, J. Opt. Soc. Am. B. **11**, 2206 (1994).
6. P. O'Shea, M. Kimmel, X. Gu, and R. Trebino, Opt. Lett. **26**, 932 (2001).
7. C. Iaconis and I. A. Walmsley, Opt. Lett. **23**, 792 (1998).
8. P. Baum, S. Lochbrunner, and E. Riedle, Opt. Lett. **29**, 210 (2004).
9. M. Hirasawa, N. Nakagawa, K. Yamamoto, R. Morita, H. Shigekawa, and M. Yamashita, Appl. Phys. B. **74**, s225 (2002).
10. C. Dorrer, P. Londero, and I. A. Walmsley, Opt. Lett. **26**, 1510 (2001).
11. A. Monmaryrant, M. Joffre, T. Oksenhendler, R. Herzog, D. Kaplan, and P. Tournois, Opt. Lett. **28**, 278 (2003).
12. E. M. Kosik, A. S. Radunsky, I. A. Walmsley, and C. Dorrer, Opt. Lett. **30**, 326 (2005).
13. Z. Guang, M. Rhodes, M. Davis, and R. Trebino, J. Opt. Soc. Am. B **31**, 2736 (2014).
14. M. Louisy, C. Guo, L. Neoričić, S. Zhong, A. L'Huillier, C. L. Arnold, and M. Miranda, Appl. Opt. **56**, 9084 (2017).
15. K. Y. Kim, I. Alexeev, and H. M. Milchberg, Appl. Phys. Lett. **81**, 4124 (2002).
16. J. K. Wahlstrand, S. Zahedpour, and H. M. Milchberg, J. Opt. Soc. Am. B **33**, 1476 (2016).
17. D. Patel, D. Jang, S. W. Hancock, H. M. Milchberg, and K. Y. Kim, Optics Express **28**, 11023 (2020).
18. S. P. Le Blanc, E. W. Gaul, N. H. Matlis, A. Rundquist, and M. C. Downer, Opt. Lett. **25**, 764 (2000).
19. J. P. Geindre, P. Audebert, A. Rousse, F. Falliès, J. C. Gauthier, A. Mysyrowicz, A. Dos Santos, G. Hamoniaux, and A. Antonetti, Opt. Lett. **19**, 1997 (1994).
20. J. K. Wahlstrand, S. Zahedpour, A. Bahl, M. Kolesik, and H. M. Milchberg, Phys. Rev. Lett. **120**, 183901 (2018).
21. Y. H. Chen, S. Varma, A. York, and H. M. Milchberg, Opt. Express **15**, 11341 (2007).
22. J. K. Wahlstrand, S. Zahedpour, Y.-H. Cheng, J. P. Palastro, and H. M. Milchberg, Phys. Rev. A **92**, 063828 (2015).
23. S. Zahedpour, S. W. Hancock, and H. M. Milchberg, Opt. Lett. **44**, 843 (2019).
24. S. W. Hancock, S. Zahedpour, A. Goffin, and H. M. Milchberg, Optica **6**, 1547 (2019).
25. N. Jhajj, I. Larkin, E. W. Rosenthal, S. Zahedpour, J. K. Wahlstrand, and H. M. Milchberg, Phys. Rev. X **6**, 031037 (2016).
26. L. Allen, M. W. Beijersbergen, R. J. C. Spreeuw, and J. P. Woerdman, Phys. Rev. A. **45**, 8185 (1992).
27. M. A. Porras, Phys. Rev. Lett. **122**, 123904 (2019).
28. L. Marrucci, C. Manzo, and D. Paparo, Phys. Rev. Lett. **96**, 163905 (2006).
29. S. Carbajo, E. Granados, D. Schimpf, A. Sell, K.-H. Hong, J. Moses, and F. X. Kärtner, Opt. Lett. **39**, 2487 (2014).
30. J. P. Heritage, R. N. Thurston, W. J. Tomlinson, A. M. Weiner, and R. H. Stolen, Appl. Phys. Lett. **47**, 87 (1985).
31. A. M. Weiner, J. P. Heritage, and E. M. Kirschner, J. Opt. Soc. Am. B. **5**, 1563 (1988).
32. A. M. Weiner and D. E. Leaird, Opt. Lett. **15**, 51 (1990).
33. N. Jhajj, "Hydrodynamic and electrodynamic implications of optical femtosecond filamentation," Ph.D. dissertation (University of Maryland, 2017).
34. S. Zahedpour, S. W. Hancock, and H. M. Milchberg, in *Frontiers in Optics + Laser Science APS/DLS, OSA Technical Digest* (Optical Society of America, 2019), paper FW5F.5.
35. W. R. Klein and B. D. Cook, IEEE Trans. Sonics Ultrason. **14**, 123 (1967).
36. A. Couairon, E. Brambilla, T. Corti, D. Majus, O. de J. Ramırez-Gongora, and M. Kolesik, Eur. Phys. J. Spec. Top. **199**, 5 (2011).
37. M. Kolesik and J. V. Moloney, Phys. Rev. E. **70**, 036604 (2004).
38. M. Takeda, H. Ina, and S. Kobayashi, J. Opt. Soc. Am. **72**, 156 (1982).
39. S. W. Hancock, S. Zahedpour, and H. M. Milchberg, in *Frontiers in Optics + Laser Science APS/DLS*, OSA Technical Digest (Optical Society of America, 2020), paper FM7C.6.
40. S. W. Hancock, S. Zahedpour, and H. M. Milchberg, in *High-Brightness Sources and Light-Driven Interactions Congress*, OSA Technical Digest (Optical Society of America, 2020), paper JM3A.21.